The Astrophysical Journal, 810:62 (14pp), 2015 September 1 doi:10.1088/0004-637X/810/1/62

A COMBINED *SPITZER* AND *HERSCHEL* INFRARED STUDY OF GAS AND DUST IN THE CIRCUMBINARY DISK ORBITING V4046 Sgr

Valerie A. Rapson[1], Benjamin Sargent[1], G. Germano Sacco[2], Joel H. Kastner[1], David Wilner[3], Katherine Rosenfeld[3], Sean Andrews[3], Gregory Herczeg[4], and Nienke van der Marel[5]
[1] School of Physics and Astronomy, Rochester Institute of Technology, 1 Lomb Memorial Drive, Rochester, NY 14623-5603, USA; var5998@rit.edu
[2] INAF-Arcetri Astrophysical Observatory, Largo Enrico Fermi 5, I-50125 Florence, Italy
[3] Harvard-Smithsonian Center for Astrophysics, 60 Garden Street, Cambridge, MA 02138, USA
[4] Kavli Institute for Astronomy and Astrophysics, Peking University, Yi He Yuan Lu 5, Haidian Qu, Beijing 100871, China
[5] Leiden Observatory, Leiden University, P.O. Box 9513, 2300 RA, Leiden, The Netherlands
Received 2014 December 1; accepted 2015 July 20; published 2015 August 31

ABSTRACT

We present results from a spectroscopic *Spitzer* and *Herschel* mid-to-far-infrared study of the circumbinary disk orbiting the evolved (age ∼12–23 Myr) close binary T Tauri system V4046 Sgr. *Spitzer* InfraRed Spectrograph spectra show emission lines of [Ne II], H_2 S(1), CO_2, and HCN, while *Herschel* Photodetector Array Camera and Spectrometer and Spectral and Photometric Imaging Receiver spectra reveal emission from [O I], OH, and tentative detections of H_2O and high-J transitions of CO. We measure [Ne III]/[Ne II] $\lesssim 0.13$, which is comparable to other X-ray/EUV luminous T Tauri stars that lack jets. We use the H_2 S(1) line luminosity to estimate the gas mass in the relatively warm surface layers of the inner disk. The presence of [O I] emission suggests that CO, H_2O, and/or OH is being photodissociated, and the lack of [C I] emission suggests any excess C may be locked up in HCN, CN, and other organic molecules. Modeling of silicate dust grain emission features in the mid-infrared indicates that the inner disk is composed mainly of large ($r \sim 5\ \mu$m) amorphous pyroxene and olivine grains (∼86% by mass) with a relatively large proportion of crystalline silicates. These results are consistent with other lines of evidence indicating that planet building is ongoing in regions of the disk within ∼30 AU of the central, close binary.

Key words: circumstellar matter – infrared: stars – line: identification – stars: low-mass – stars: pre-main sequence

1. INTRODUCTION

The relatively rare examples of nearby T Tauri stars (i.e., those within ∼100 pc of Earth) are excellent candidates for studying planet formation processes. Their proximity allows us to analyze the contents and structure of circumstellar disks in which young protoplanets are likely forming. Near- to far-infrared spectroscopy allows us to probe the contents of these protoplanetary disks, as the strongest emission from such disks arises at infrared and (sub-)millimeter wavelengths. Mid-IR (5–40 μm) spectroscopy traces both the gas and dust components of the inner ($R < 10$ AU) planet-forming regions of the disk. At medium to high resolution, we detect emission features due to increasing disk temperature from the disk midplanes to their exteriors (Calvet et al. 1991; Malbet & Bertout 1991). In most cases, such spectral features only probe the disk atmosphere, as the disk becomes optically thick toward the midplane. Emission features may also arise from optically thin regions of the disk due to dust sublimation or grain growth and planetesimal formation (Pontoppidan et al. 2014). Transition disks with an inner gap carved out by giant planet formation and/or disk photoevaporation may display cavity walls with emission features due to being directly exposed to stellar UV radiation (e.g., Cleeves et al. 2011). Far-IR (50–700 μm) spectroscopy traces emission from colder gas and dust in the outer ($R \gtrsim 10$ AU) disk. At these longer wavelengths, we expect emission features from gas-mass tracers such as CO and atomic species that trace photodissociation regions at disk surfaces.

Previous *Spitzer Space Telescope* and ground-based mid-IR spectroscopic studies of pre-main-sequence (pre-MS) star/disk systems have revealed a variety of atomic and molecular emission features (e.g., Pontoppidan et al. 2010; Salyk 2011). Molecules such as C_2H, HCN, CN, OH, H_2O, and C_2H_2, whose abundances are sensitive to stellar UV and X-ray radiation, are used to gauge the strength of disk gas photodissociation and radiative heating processes (e.g., Bergin et al. 2003; Pascucci et al. 2009, 2013; Henning et al. 2010). H_2O has also been observed in the planet-forming regions around many young stars (e.g., Salyk et al. 2011). Metal ions such as [Ne II] have also been detected toward transitional disks (Lahuis et al. 2007; Pascucci et al. 2007; Güdel et al. 2010; Sacco et al. 2012) and may trace the influence of high-energy radiation on disk photoevaporation rates.

Far-IR spectroscopic observations of pre-MS star/disk systems via the *Herschel* space observatory help constrain the disk gas and dust mass, as well as the effects of high-energy radiation on outer disk heating and chemistry (e.g., Thi et al. 2010; Howard et al. 2013; Fedele et al. 2013; Meeus et al. 2013; Riviere-Marichalar et al. 2013). Far-IR emission from pure rotational CO lines probe temperature regimes between those of the near-IR vibrational CO lines and the low-J sub-millimeter/radio CO lines and can reveal information about this distribution of gas throughout the disk (e.g., Bruderer et al. 2012). The presence of far-IR [O I], [C I], and [C II] emission lines may indicate that UV or X-ray radiation is incident on the outer disk and photodissociating CO or OH molecules (Mamon et al. 1988; Aresu et al. 2012). Modeling these and other diagnostic emission lines in *Herschel* spectra, combined with models of *Spitzer* spectroscopic observations, can constrain total disk mass, as well as the composition and distribution of gas and dust throughout the disk.

Here, we present a combined spectroscopic *Spitzer* and *Herschel* study of the protoplanetary disk orbiting the nearby

($D \sim 73$ pc; Torres et al. 2008) pre-MS binary V4046 Sgr. V4046 Sgr is an isolated, spectroscopic binary that is a member of the β Pic Moving Group, with an age of ~12–23 Myr (Torres et al. 2006; Binks & Jeffries 2013; Mamajek & Bell 2014). The binary consists of nearly equal mass components with spectral types K5Ve and K7Ve (Stempels & Gahm 2004) and a total mass 1.75 $M_{\odot}$ (Rosenfeld et al. 2012a). The stars are separated by 0.04 AU ($p \sim$ 2.4 days; Stempels & Gahm 2004) and are surrounded by a large ($R \sim 370$ AU) circumbinary disk of gas and dust inclined at ~33° from face-on (Rodriguez et al. 2010; Rosenfeld et al. 2012a). The central stars are actively accreting material (Stempels & Gahm 2004; Donati et al. 2011; Argiroffi et al. 2012) from the disk, which has an inner gap of radius ~30 AU that is possibly due to ongoing Jovian planet formation (Rosenfeld et al. 2013). The disk is also evidently undergoing photoevaporation by high-energy radiation from the central stars (Sacco et al. 2012), which, in conjunction with planet formation, may contribute to the inner disk clearing (Alexander et al. 2014 and references therein).

In this paper, we present a census of atomic and molecular emission features detected in the *Spitzer* and *Herschel* spectra of V4046 Sgr, and we model the continuum of the *Spitzer* spectrum to determine the dust particle composition of the disk. Our *Spitzer* and *Herschel* observations and data reduction processes are discussed in Section 2, and in Sections 3 and 4, we report the results of our emission line study. In Section 5, we discuss our modeling of the dust features in the *Spitzer* spectrum, and we present a summary of our conclusions in Section 6.

2. OBSERVATIONS AND DATA REDUCTION

2.1. Spitzer InfraRed Spectrograph (IRS)

Low ($R \sim$ 60-130) and high ($R \sim 600$) resolution *Spitzer Space Telescope* (Werner et al. 2004) data for V4046 Sgr were obtained with the IRS (Houck et al. 2004) in 2005 April (PI: Mitsuhiko Honda)[6] and were retrieved through the *Spitzer* Heritage Archive. Short low (SL, 5–20 μm), short high (SH, 10–20 μm), and long high (LH, 20–37 μm) data were reduced individually using SMART v8.2.5 (Higdon et al. 2004). No background subtraction or low-level rogue pixel removal was performed on the high-resolution data because no dedicated background images were available. All images were manually examined after processing and bad pixels (particularly near 6.9 and 17.6 μm) were smoothed over.

The two nods of each set of cleaned spectra were averaged together, and the three modes were combined using custom IDL programs. SL data are available for the ~5–14 μm range, but are used only in the 5–10 μm range, where high-resolution data are not available. Examination of the original spectra showed a relatively smooth continuum, with a small jump between the SH and LH spectra at ~20 μm. As V4046 Sgr is unresolved by *Spitzer*, this mismatch is likely due to the source falling off the slit in the SH module. Hence, the SL and SH spectra were scaled by a multiplicative factor of 1.182 such that the SL and SH matched the LH spectra at ~20 μm. The resulting *Spitzer* spectrum (5–35 μm) is shown in Figure 1. It is possible that the excess flux in the LH spectrum is due to residual sky background. If this is the case, then the LH spectra should be scaled down by 1.182 to match that of the SH and SL spectra.

[6] Program ID: 3580, AORKEY: 11197440.

2.2. Herschel Photodetector Array Camera and Spectrometer (PACS) and Spectral and Photometric Imaging Receiver (SPIRE)

Herschel Space Observatory (Pilbratt et al. 2010) PACS (Poglitsch et al. 2010) range scan spectra and SPIRE (Griffin et al. 2010) spectra of V4046 Sgr were obtained as part of the Cycle 1 General Observer Program[7] (PI: G. Sacco) in 2012 June and July. SPIRE data were obtained at medium resolution ($R \sim$ 160), and PACS data were obtained in spectral energy distribution (SED) mode ($R \sim$ 940–5500). Together, these observations cover the 55–670 μm range. Examination of the SPIRE level 2 data products showed a discontinuity between the two bands (190–310 and 300–670 μm), suggesting that the background was incorrectly subtracted by the pipeline.[8] We therefore reduced both the PACS and SPIRE data from level 0 in HIPE v10 (Ott 2010) using interactive background normalization scripts, which allow us to subtract the background more accurately than is done in the standard pipeline. Data from calibration trees 48 and 10.1 for PACS and SPIRE, respectively, were used to correct for instrumentation effects and to flux calibrate the spectra. The center spatial pixel (spaxel) was extracted from the resulting 5x5 spaxel array and order edges, and regions in the spectrum where light leakage occurs were removed. The resulting *Herschel* PACS and SPIRE data are shown in Figures 2 and 3.

Herschel PACS line scan spectra were obtained in Cycle 2[9] (P. I. G. Herczeg) in 2013 June with the goal of searching for mid- to high-J lines of CO, as well as H_2O and OH. These data cover eight different wavelength regions. The PACS line scan data were reduced from level 0 using background normalization scripts in HIPE v11 with PACS calibration tree 56. Two output spectra were produced, one that was flux calibrated using the central 3x3 spaxel region and one that was not. Telescope jitter and slight pointing errors can cause some of the source flux in *Herschel* observations to extend beyond the central spaxel. This effect can be corrected by taking the flux ratio of the sum of the central 3×3 spaxels to the single center spaxel and comparing it with the ratio of a perfectly pointed observation of a point source, then adjusting the source flux accordingly. A comparison between the 3×3 corrected spectra and the non-corrected spectra shows a ~10% difference in continuum flux values. Since this difference is small, and since the PACS SED spectra were not 3×3 corrected, we chose to use the non-3×3 corrected spectra. The continuum flux of the PACS line scan and SED data for each region also matched to within ~10%, consistent with the level of systematic error. The PACS line scan spectra are shown in Figure 4.

3. ANALYSIS: GAS EMISSION FEATURES

3.1. Emission Line Identification

Spectral line identification in both the *Spitzer* and *Herschel* spectra was performed both by eye and using custom IDL programs. To identify potential lines in the IRS spectrum, we first fit the continuum regions of the SH and LH data with a

[7] Observation IDs: 1342231043, 1342242448, 1342242449.
[8] See Section 6.4 in the SPIRE data reduction Guide v2.1.
[9] Observation IDs: 1342269454 and 1342269455.

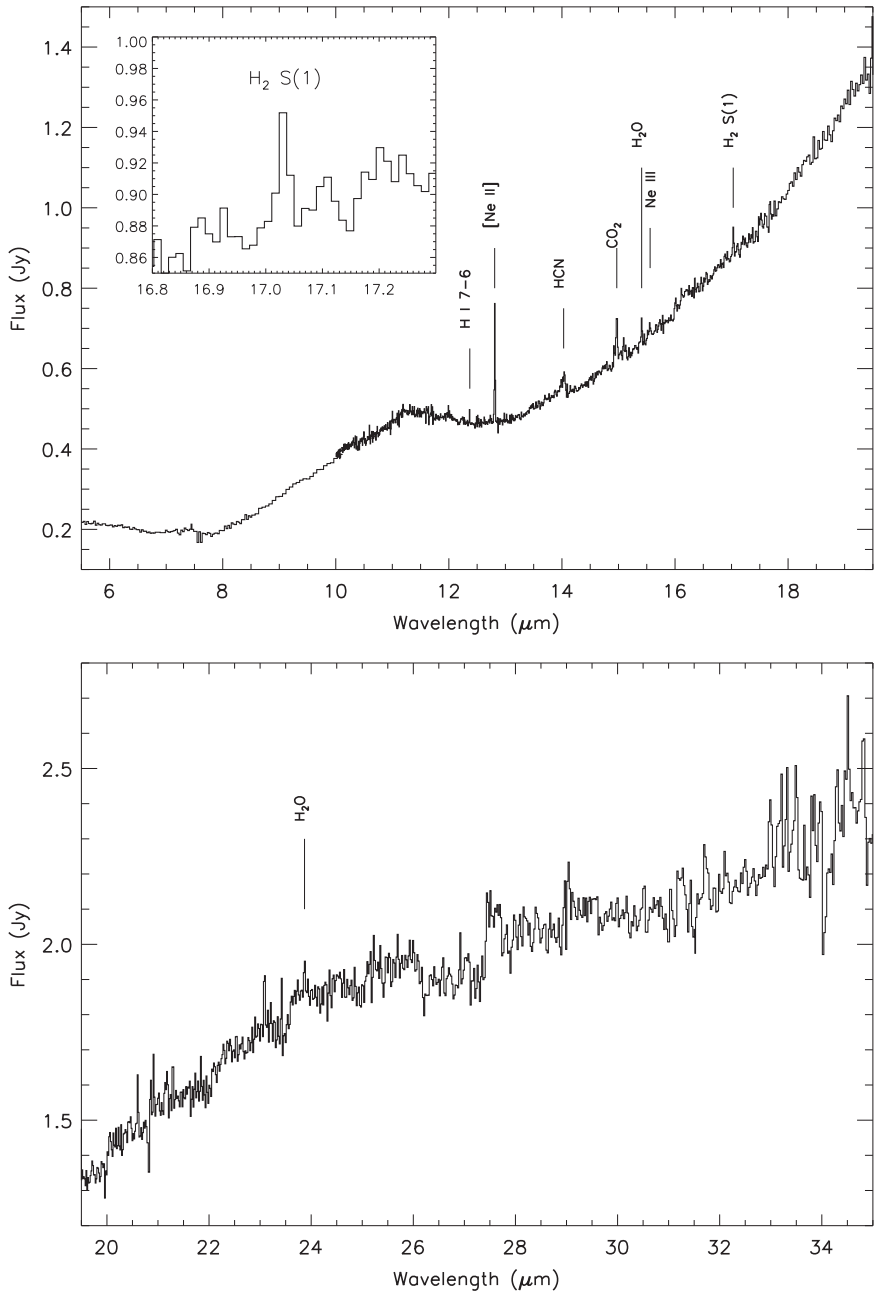

Figure 1. *Spitzer* IRS spectrum of V4046 Sgr with emission features labeled. Top: 5.5–19.5 μm spectrum with an inset showing the H_2 0-0 S(1) ($J = 3 \rightarrow 1$) line at 17.035 μm. Bottom: 19.5–35 μm spectrum with emission features labeled.

high-order polynomial, then subtracted the data from the fitted continuum. We then identified candidate emission lines as features that span at least two spectral bins and are at least 2σ above the continuum (where σ is defined as the standard deviation of the continuum-subtracted spectra). To confirm which of these detections are likely emission lines and not spurious detections or dust features, we subtract the continuum dust model (see Section 3.1) from the original spectra and repeat the above line detection process. The NIST atomic spectral database,[10] the Splatalogue database for astronomical spectroscopy,[11] and previous publications pertaining to mid- to far-infrared emission features from protoplanetary disks were used to determine the species and transition potentially associated with each candidate emission feature. We restrict these identifications to spectral features that are at least 2σ above the continuum and that correspond to molecular or atomic features previously identified in protoplanetary disks. Table 1 lists the candidate lines identified in the *Spitzer* spectrum and their measured wavelengths, energies, fluxes, FWHM, and equivalent widths.

Emission features in the *Herschel* PACS and SPIRE spectra were determined in a similar fashion. The *Herschel* PACS range scan and SPIRE spectra are less sensitive than the *Spitzer* and PACS line spectra, and thus only a few candidate emission features are identified at levels $>3\sigma$. Table 2 lists the candidate lines identified in all *Herschel* spectra and their measured wavelengths, energies, fluxes, FWHM, and equivalent widths.

[10] http://physics.nist.gov/PhysRefData/ASD/lines_form.html
[11] http://splatalogue.net/

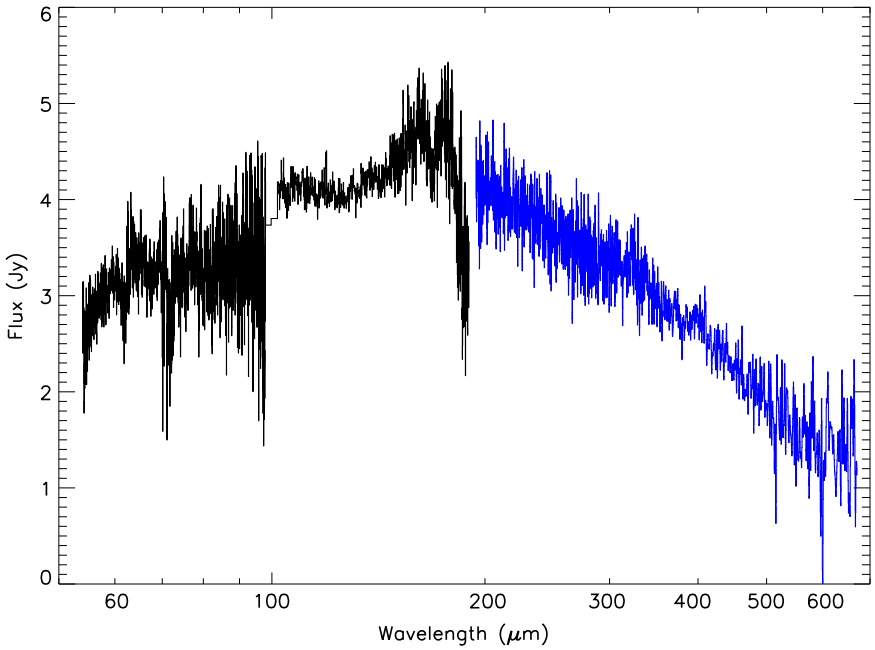

Figure 2. Top: *Herschel* PACS (black) and SPIRE (blue) spectra of V4046 Sgr. The data have been rebinned by a factor of three.

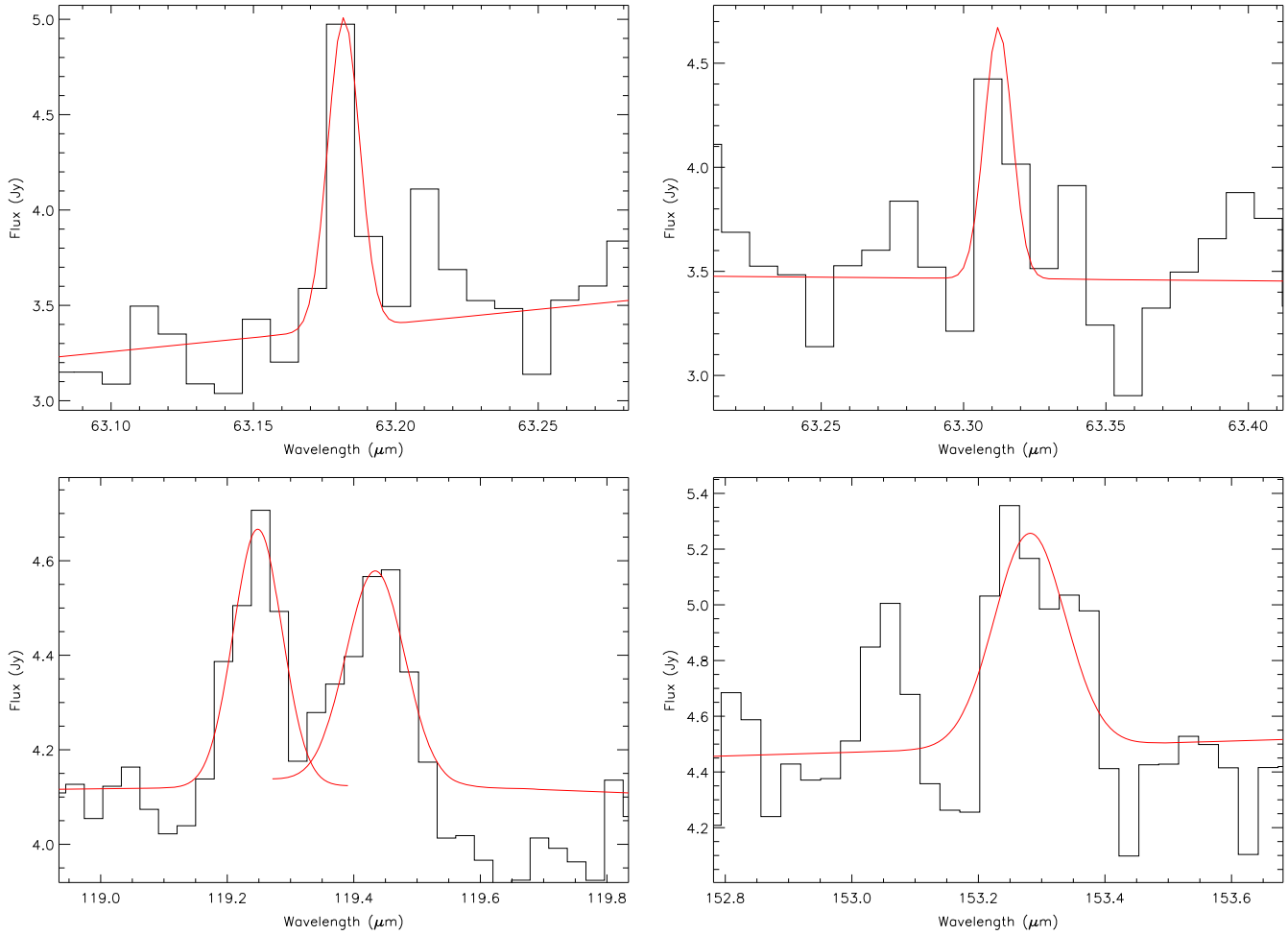

Figure 3. [O I] (top left), o-H_2O (top right), OH $^2\Pi_{3/2}$ $J = \frac{3}{2} \rightarrow \frac{5}{2}$ (bottom left), and CO $J = 17 \rightarrow 16$ (bottom right) emission features detected (or tentatively detected) in the unbinned V4046 Sgr Herschel PACS SED spectrum with Gaussian fits overlaid (red).

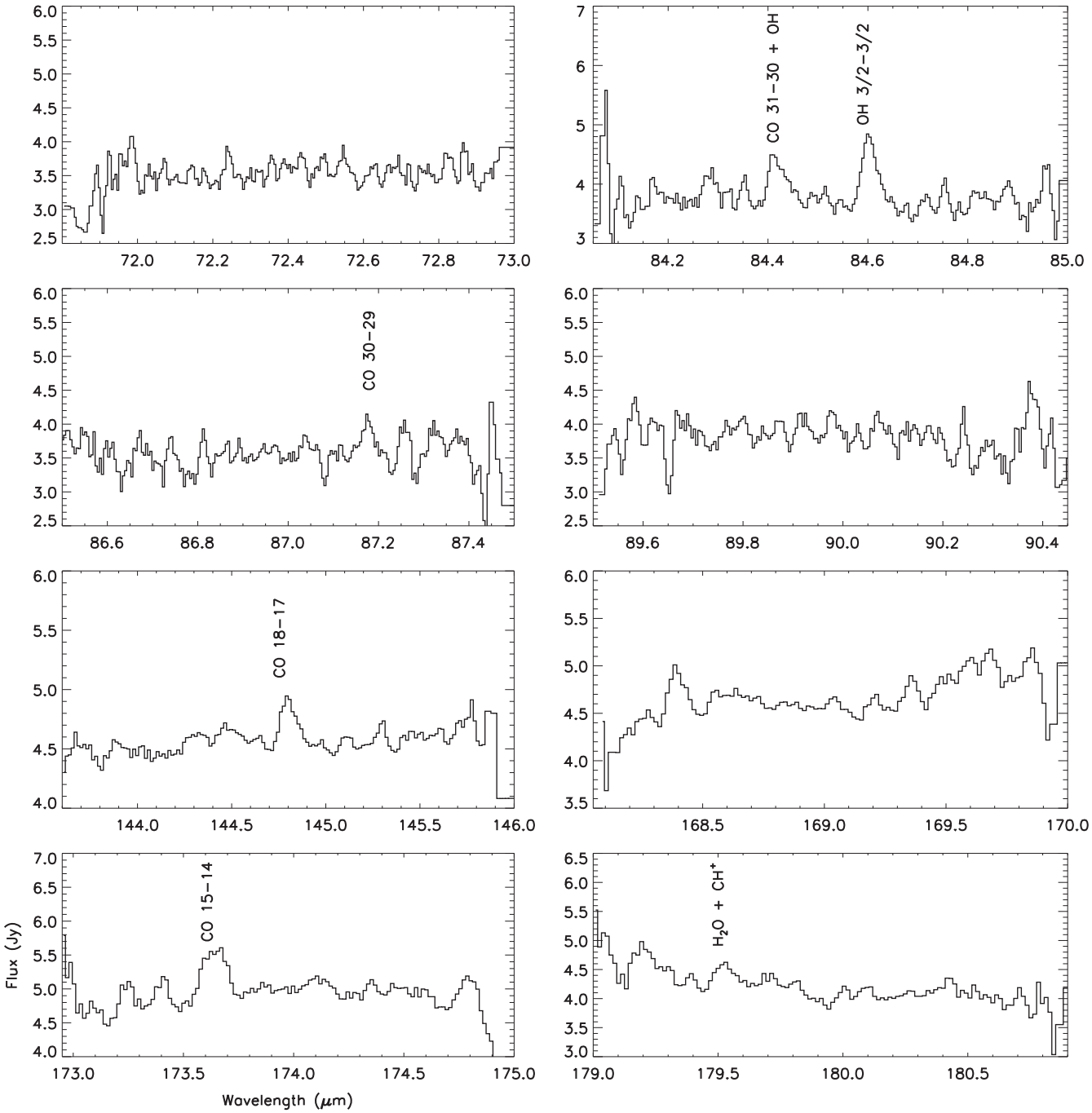

Figure 4. *Herschel* PACS line scan spectroscopy data with emission features labeled.

3.1.1. Spitzer IRS Molecular and Atomic Line Inventory

The disk around V4046 Sgr shows evidence for many different atomic and molecular species (Figures 1 and 5 and Table 1). We detect strong emission from [Ne II], as well as emission lines of H_2 S(1), CO_2, and HCN in the *Spitzer* spectrum. Emission lines of these species are commonly seen in T Tauri star/disk systems (e.g., Najita et al. 2008; Salyk et al. 2008, 2011; Pascucci et al. 2009, 2013; Pontoppidan et al. 2010). The *Spitzer* spectrum also shows H I 7-6 emission at 12.4 μm, which likely does not originate within the disk but, rather, arises from the accretion shock regions at the (binary) central stars and/or from their stellar coronae (Pascucci et al. 2007; Rigliaco et al. 2015).

Emission lines from H_2O at 15.2 and 17.2 μm, which are often used as markers to establish that a disk is water-rich (e.g., Pontoppidan et al. 2010), are not evident in the *Spitzer* spectrum of V4046 Sgr. The spectrum may display H_2O features at 15.4 and 23.9 μm, as well as possible complexes of H_2O features near 25 and 31 μm (see Figure 1). The detailed, self-consistent modeling of H_2O and OH emission required to confirm these identifications will be pursued in follow-up work. V4046 Sgr also shows HCN emission at 14.03 μm, but lacks the C_2H_2 emission lines typically found in younger T Tauri systems (Carr & Najita 2008; Salyk et al. 2011). Pontoppidan et al. (2010) and Salyk et al. (2011) find that H_2O, OH, and other molecular gas emission lines originating from warm gas

Table 1
Emission Lines in *Spitzer* IRS Spectrum of V4046 Sgr

Species	Wavelength[a] (μm)	E_u (K)	Flux (10^{-14} erg s^{-1} cm^{-2})	FWHM (10^{-2} μm)	EW (10^{-3} μm)
H I 7-6	12.37	154854	0.61 ± 0.17	0.32 ± 0.09	0.65 ± 0.18
Ne II	12.81	1124	8.67 ± 0.13	1.51 ± 0.02	10.00 ± 0.15
HCN	14.03	⋯	4.90 ± 0.38	8.00 ± 0.61	5.90 ± 0.45
CO_2	14.97	⋯	4.31 ± 0.25	2.77 ± 0.16	5.06 ± 0.30
H_2O 16-15[b]	15.41	3602	1.49 ± 0.22	1.80 ± 0.27	1.76 ± 0.26
Ne III[b]	15.55	927	<1.11	⋯	⋯
H_2 S(1)	17.03	1015	1.50 ± 0.24	2.00 ± 0.33	1.62 ± 0.27
H_2O 9-8[b]	23.86	1397	1.79 ± 0.51	2.74 ± 0.79	1.80 ±0.52

Notes.
[a] Observed wavelength.
[b] Tentative detection.

Table 2
Emission Lines in all *Herschel* Spectra of V4046 Sgr

Species	Wavelength[a] (μm)	E_u (K)	Flux (10^{-14} erg s^{-1} cm^{-2})	FWHM (10^{-2} μm)	EW (10^{-3} μm)
PACS SED					
[O I] $^3P_1 \rightarrow {}^3P_2$	63.18	228	1.71 ± 0.43	1.30± 0.33	6.72 ± 1.71
o-H_2O 8–7[b]	63.31	1071	1.09 ± 0.27	1.14 ± 0.28	4.181 ± 1.03
OH $^2\Pi_{3/2}$ $J = \frac{5}{2} - \frac{3}{2}$	119.25	121	1.11 ± 0.13	9.05 ± 0.91	12.74 ± 1.28
OH $^2\Pi_{3/2}$ $J = \frac{5}{2} - \frac{3}{2}$	119.43	121	1.10 ± 0.12	10.92 ± 1.20	12.65 ± 1.40
CO J = 17–16[b]	153.28	846	1.38 ± 0.25	13.23 ± 2.36	24.05 ± 4.29
PACS Line-scan					
OH $^2\Pi_{3/2}$ $J = \frac{7}{2} - \frac{5}{2}$ + CO J = 31–30	84.42	⋯	1.03 ± 0.05	3.30 ± 0.15	6.49 ± 0.29
OH $^2\Pi_{3/2}$ $J = \frac{7}{2} - \frac{5}{2}$	84.60	291	1.69 ± 0.05	3.29 ± 0.09	11.00 ± 0.30
CO J = 30–29[b]	87.18	2565	0.72 ± 0.06	3.23 ± 0.26	5.21 ± 0.41
CO J = 18–17	144.80	945	0.52 ± 0.22	8.78 ± 0.38	8.02 ± 0.34
CO J = 15–14	173.64	664	0.84 ± 0.02	10.98 ± 0.28	17.12 ± 0.44
o-H_2O $2_{1,2}$–$1_{0,1}$ + CH^+	179.53	114	0.23 ± 0.03	6.72 ± 0.99	5.89 ± 0.87
SPIRE					
C I	370.30	63	<0.64	⋯	⋯

Notes.
[a] Observed wavelength.
[b] Tentative detection.

in the inner disk are weaker in most transitional disk systems, likely because these disks are beginning to form an inner disk clearing either due to planet formation or disk photoevaporation. Therefore, the lack of strong H_2O and OH emission lines, and the generally weak levels of molecular emission in V4046 Sgr, are consistent with the fact that this system is a transitional disk with an inner clearing (Rosenfeld et al. 2013).

3.1.2. Herschel PACS+SPIRE Molecular and Atomic Line Inventory

Emission features in the *Herschel* PACS SED and SPIRE spectra and line IDs are presented in Figures 2 and 3 and Table 2. The *Herschel* spectra were obtained with the goal of searching for emission from [O I] at 63 μm and [C I] at 370 μm arising from UV photodissociation of CO molecules in the outer disk (Mamon et al. 1988). We report the detection of [O I] emission (Table 2 and Figure 3), but did not detect [C I]. We also detect emission from an OH 3/2–3/2 doublet at 119.2 and 119.4 μm (Figure 3), which likely arises from UV photodissociation of H_2O in the outer disk. One high-level CO ro-vibrational transition (J = 17 → 16) is tentatively detected and 3σ upper limits for all other ro-vibrational transitions of CO between 65 and 600 μm range from 0.42 to 4.68 10^{-14} erg s^{-1} cm^{-2}.

The *Herschel* PACS line scan spectra cover multiple limited spectral regions also spanned by PACS range spectroscopy, but achieved higher sensitivity and spectral resolution. These observations reveal several emission features that were below the detection limit of the PACS SED data (Figure 4 and Table 2). Specifically, we detect (or tentatively detect) emission from four high-level CO ro-vibrational transitions (J = 31 → 30, 30 → 29, 18 → 17, and 15 → 14), as well as OH

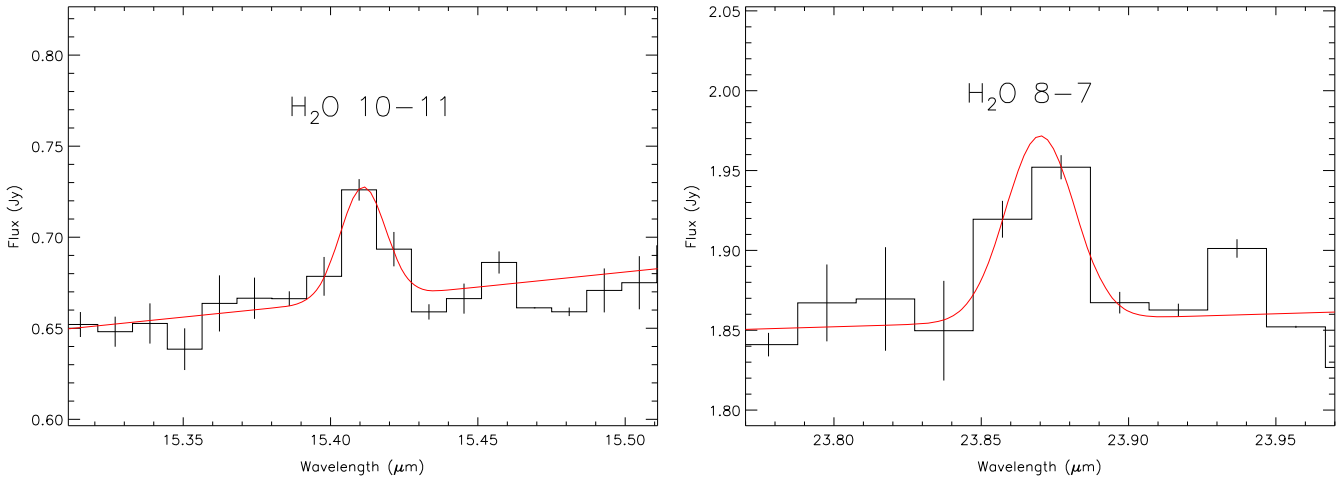

Figure 5. H_2O emission features tentatively detected in the *Spitzer* IRS spectrum of V4046 Sgr with Gaussian fits overlaid.

and CH^+. The PACS line scan spectra do not cover the spectral range in which emission features were detected in the PACS SED spectra, so we cannot use these data to confirm the existence of the H_2O and CO $J = 17 \rightarrow 16$ features.

4. DISCUSSION: GAS EMISSION FEATURES

V4046 Sgr exhibits emission features that allow us to further understand the structure, content, and chemistry of the circumbinary disk. We can use these emission features to investigate disk photoevaporation and photodissociation processes and to compare the V4046 Sgr system with other similarly evolved systems such as TW Hya (age $\sim$8 Myr, $d \sim 53$ pc; Ducourant et al. 2013 and references therein) and other T Tauri star–disk systems in nearby associations. Below, we comment on notable features in the *Spitzer* and *Herschel* spectra of V4046 Sgr and combine the *Spitzer* and *Herschel* spectra to obtain a full mid- to far-IR SED (5–670 μm) so as to compare the SED with a dust disk model from Rosenfeld et al. (2013).

4.1. H_2

Although H_2 is the most abundant species in circumstellar disks, the electric quadrupole nature of its rotational transitions result in weak emission that is difficult to detect. However, pure rotational H_2 emission has been detected in the mid-IR around some T Tauri and Herbig Ae/Be stars (i.e., Lahuis et al. 2007; Bary et al. 2008; Bitner et al. 2008; Carmona et al. 2008; Najita et al. 2010; Carr & Najita 2011) and even in a few disks around young brown dwarfs (Pascucci et al. 2013). This emission may be due to collisional excitation, X-ray/UV irradiation of the disk surface, and/or accretion shocks onto the disk (Bitner et al. 2008 and references therein).

We detect emission from pure rotational H_2 0-0 S(1) ($J = 3 \rightarrow 1$) at 17.035 μm in the *Spitzer* spectrum (Table 1). Since V4046 Sgr lies far from any molecular clouds (Kastner et al. 2008), the H_2 emission most likely arises from warm gas in the surface layers of the circumbinary disk. The line flux of H_2 is $\sim 1.50 \times 10^{-14}$ erg s^{-1} cm^{-2} ($L_{H_2} = 1.04 \times 10^{28}$ erg s^{-1}). This is comparable to the 17 μm H_2 line strengths measured in T Tauri stars studied by Bitner et al. (2008), as well as to the 17 μm H_2 line luminosity from the (similarly isolated) TW Hya ($L_{H_2} = 4.17 \times 10^{27}$ erg s^{-1}, assuming a distance of 53 pc; Najita et al. 2010).

Carmona et al. (2008) did not detect H_2 emission toward V4046 Sgr using VISIR on the Very Large Telescope (VLT) Melipal telescope. They report a three sigma upper limit for 17 μm H_2 emission of $<1.3 \times 10^{-14}$ erg s^{-1} cm^2, which is roughly equivalent to our measured H_2 17 μm flux. The non-detection of H_2 by Carmona et al. (2008) may be due to VISIR having a smaller slit size or the difficulty of removing atmospheric effects from ground-based spectra. It is also possible that the H_2 emission is variable as a result of ongoing accretion and variable X-ray/UV luminosity (Bary et al. 2008).

Assuming that the H_2 emission is optically thin, the H_2 gas is in local thermal equilibrium, and the IRS slit covers the entire source (note that we have already corrected for the source possibly extending beyond the coverage of the SH slit), we can estimate an upper limit for the mass of the emitting H_2 gas as a function temperature from

$$M_{\rm gas} = f \times 1.76 \times 10^{-20} \frac{4\pi d^2 \lambda F_{ul}}{hcA_{ul}x_u(T)} M_\odot, \quad (1)$$

where F_{ul} is the flux of the H_2 emission line, λ is the central wavelength of the emission line, d is the distance in parsecs, A_{ul} is the Einstein coefficient of the $J = u$–l transition,[12] and $x_u(T)$ is the population at level u for a given excitation temperature T (Thi et al. 2001). Since only the H_2-ortho 17 μm emission line is detected in our spectrum, we multiply by a conversion factor $f = 1 + (\text{ortho/para})^{-1}$ (Carmona et al. 2008), where the equilibrium ortho/para ratio can be determined from Equation (1) in Takahashi (2001).

Figure 6 shows the resulting mass of the emitting H_2 gas for various excitation temperatures, as well as the total gas+dust mass of the disk established by Rosenfeld et al. (2013; 0.094 $M_\odot$). It is apparent that if the H_2 gas were at temperatures $\lesssim$100 K, the gas mass needed to produce the line flux we see in the *Spitzer* spectrum would exceed that of the total gas+dust disk mass. Indeed, from the upper limit on the flux of the H_2 S (0) emission feature at 28.2 μm ($<1.9 \times 10^{-14}$ erg s^{-1} cm^{-2}), we estimate the lower limit for the excitation temperature of the

[12] $A_{ul} = 4.76 \times 10^{-10}$ s^{-1}. for the H_2-ortho $J = 3$–1 transition (Wolniewicz et al. 1998).

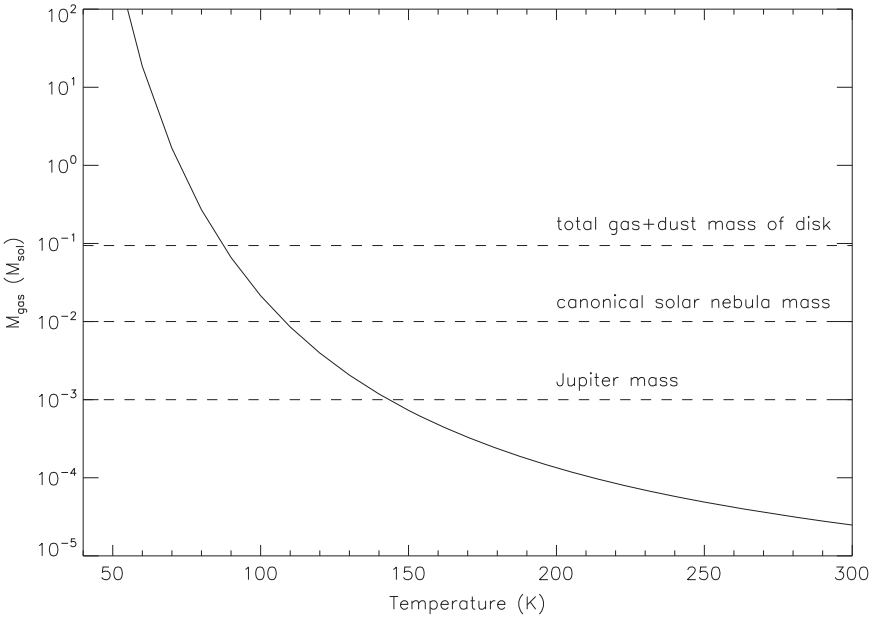

Figure 6. H_2 gas mass inferred from the strength of the 17 μm S(1) emission line as a function of temperature (solid curve). The horizontal dashed lines represent the masses of Jupiter, canonical solar nebula, and the total gas+dust mass of the disk around V4046 Sgr (Rosenfeld et al. 2013).

H_2 emitting gas to be ~100 K (see Thi et al. 2001, Equation (3)). This suggests that much of the IR emitting H_2 gas resides in the surface layers of the disk, where the temperature is warmer than the midplane at a given radius due to stellar X-ray and/or UV irradiation.

4.2. *[Ne II] and [Ne III]*

The brightest line in the *Spitzer* IRS spectrum of V4046 Sgr is that of [Ne II] at 12.8 μm. We measure a [Ne II] emission flux of $8.67 \pm 0.13 \times 10^{-14}$ erg s^{-1} cm^{-2}. [Ne II] emission is often prominent in T Tauri systems and likely traces hot ($T \sim 5000$ K) disk gas that is being photoevaporated by EUV and X-ray radiation incident on the disk's upper atmosphere within a few tens of AU of the central star (Glassgold et al. 2004). Irradiated disk models (Ercolano et al. 2008; Meijerink et al. 2008; Ercolano & Owen 2010) predict a correlation between the strength of the [Ne II] line and the X-ray luminosity. Recent studies of circumstellar disks (e.g., Güdel et al. 2010; Sacco et al. 2012) have shown a weak correlation between X-ray luminosity and [Ne II], and blueshifts of [Ne II] consistent with emission due to a photoevaporative wind or magnetically driven outflow.

Sacco et al. (2012) obtained high-resolution mid-IR spectra covering the [Ne II] (12.81 μm) emission line toward V4046 Sgr (and 31 other YSOs) using the VISIR spectrograph on the VLT. They detected V4046 Sgr and measured a [Ne II] line flux of $6.6 \pm 0.2 \times 10^{-14}$ erg s^{-1} cm^{-2}. Sacco et al. (2012) also measured the flux of the [Ne II] 12.81 μm emission from the *Spitzer* spectrum as $7.68 \pm 0.22 \times 10^{-14}$ erg s^{-1} cm^{-2}, which is consistent with our flux measurement after rescaling for slit loss. The difference between the *Spitzer* and VLT [Ne II] flux measurements may be indicative of time variability of the emission, but could also be due to the different slit sizes.

The VLT [Ne II] emission from V4046 Sgr is slightly blueshifted and likely arises from a photoevaporative wind that is escaping the inner gaseous disk (Sacco et al. 2012). Rapson et al. (2015) show that the $R \sim 30$ AU gap in the disk (Rosenfeld et al. 2013) is filled with (sub-)micron dust grains that may provide enough opacity to produce the observed [Ne II] line. Calculation of the 12 μm opacity throughout the V4046 Sgr disk based on dust column densities from Rosenfeld et al. (2013) suggests that there is sufficient optical depth at $R \sim 20$–50 AU to absorb the redshifted portion of the [Ne II] emission. Thus, the [Ne II] emission likely originates in this region of the inner disk, as Sacco et al. (2012) suggested.

Espaillat et al. (2007) measure the [Ne II] emission from CS Cha, a ~2 Myr old T Tauri star that is similar to V4046 Sgr in that it is surrounded by a transitional disk with an inner gap out to $R \sim 43$ AU. V4046 Sgr has a [Ne II] luminosity of 5.5×10^{28} erg s^{-1} (assuming $D = 73$ pc), which is roughly half that measured for CS Cha. If the strength of the [Ne II] emission is due to X-ray and EUV photons impinging on the disk, then this lower [Ne II] luminosity would be consistent with the fact that the X-ray luminosity of V4046 Sgr is also lower than that for CS Cha (Feigelson et al. 1993; Donati et al. 2011). However, both disks have a [Ne II] luminosity higher than what is typically observed for classical T Tauri stars (Espaillat et al. 2007; Pascucci et al. 2007 and references therein). Espaillat et al. (2007) attribute this to the high accretion rate of CS Cha (1.2×10^{-8} $M_\odot$ yr^{-1}), yet V4046 Sgr has a much lower accretion rate (5×10^{-10} $M_\odot$ yr^{-1}; Donati et al. 2011) and still shows a high [Ne II] luminosity. Therefore, mass accretion rate may not be a good indication of the strength of the [Ne II] line in circumstellar disks. This comparison points out the need for additional studies aimed at investigating potential correlations between [Ne II] line luminosity and star/disk system parameters.

The 12.8 μm [Ne II] feature, combined with measurements of emission from [Ne III], can be used as X-ray/EUV radiation field diagnostics. Emission from 15.6 μm [Ne III] is rarely detected in T Tauri systems, and upper limits are usually an order of magnitude below that of [Ne II] (e.g., Lahuis et al. 2007). We report only an upper limit for the 15.6 μm [Ne III] line in Table 1, as this line is at best tentatively detected and a potential line is only apparent in one nod. For V4046 Sgr,

we find [Ne III]/[Ne II] $\lesssim$ 0.13, which is consistent with the ratio determined for TW Hya ([Ne III]/[Ne II] $\sim$ 0.045; Najita et al. 2010) and is comparable to other CTTS that lack jets (e.g., Lahuis et al. 2007). Modeling of X-ray irradiation of protoplanetary disks (Ercolano et al. 2008) also predicts [Ne III]/[Ne II] $\lesssim$ 0.1 for X-ray bright systems.

Pascucci et al. (2014) constrain the EUV irradiation of the V4046 Sgr disk by studying radio data that traces free–free emission from ionized gas caused by EUV irradiation. They find that the inferred EUV luminosity reaching the disk is much lower for older disks (V4046 Sgr, TW Hya, and MP Mus) than for younger, less evolved disks and that the EUV flux for V4046 Sgr is not sufficient to produce the [Ne II] luminosities measured by Sacco et al. (2012) and confirmed in this work. Thus, the disk is likely being photoevaporated by $\sim$1 keV X-ray photons at a faster rate than if EUV photons were responsible for the photoevaporation.

4.3. H_2O and OH

Emission from H_2O and OH has been detected in the *Spitzer* spectra around many young stars (e.g., Carr & Najita 2008; Salyk et al. 2008; Pontoppidan et al. 2010; Carr & Najita 2011). In general, this emission is found to arise from regions of the disk with temperatures $\lesssim$1000 K, corresponding to a radius of a few AU, where some H_2O is photodissociated into OH by far-UV photons. V4046 Sgr shows tentative evidence for H_2O emission in the *Spitzer* spectrum, but lacks emission at wavelengths that typically trace the presence of H_2O and OH in circumstellar disks (see Section 3.1.1). In particular, the *Spitzer* spectrum of TW Hya (Najita et al. 2010) shows no emission from H_2O in the *Spitzer* SH spectrum, but displays many OH emission lines.

Emission from the higher-energy rotational states ($E_{\rm upper} \gtrsim$ 7000 K) of OH observed in the TW Hya spectrum likely arises from warm ($T \sim$ 1000 K) H_2O gas that has been photodissociated within the inner 1 AU of the disk. This suggests that even though TW Hya exhibits an inner hole ($R \sim$ 4 AU) in its dusty disk (Hughes et al. 2007; Rosenfeld et al. 2012b), there is gas present within this hole in the form of dissociated water vapor. We cannot rule out the presence of OH emission in the V4046 Sgr IRS spectrum at the level of that in the TW Hya IRS spectrum because the V4046 Sgr spectrum is less sensitive (due to shorter exposure times).[13] Thus, while the lack of H_2O emission in the *Spitzer* spectrum of V4046 Sgr may be due to FUV radiation photodissociating the H_2O to form OH, more sensitive measurements and modeling of emission features are needed to confirm the presence of OH.

Emission from OH is clearly present in the *Herschel* spectra of V4046 Sgr, while o-H_2O $8_{18} \rightarrow 7_{07}$ emission at 63.32 μm (Figure 3) is tentatively detected. Howard et al. (2013), Riviere-Marichalar et al. (2012a), and Keane et al. (2014) detect ortho-H_2O $8_{18} \rightarrow 7_{07}$ emission from various T Tauri disks in the Taurus/Auriga and other nearby star-forming regions, especially from those that also display [O I] emission. Based on visual inspection of the *Herschel* spectra in Thi et al. (2010), TW Hya may also show o-H_2O emission at 63 μm, though it is not noted in that paper. Emission from 63 μm o-H_2O in T Tauri disks had been thought to originate from the same regions at which the hot H_2O gas emission in *Spitzer* spectra is present (Salyk et al. 2008; Meijerink et al. 2009; Pontoppidan et al. 2009), but recent modeling of o-H_2O emitting sources (Riviere-Marichalar et al. 2012a) has shown that the 63 μm emission originates at larger radii in the disk. Similarly detailed modeling of the emission spectrum of V4046 Sgr is needed to confirm if this is the case for V4046 Sgr; if so, it is a direct probe of cooler H_2O in the disk.

Hogerheijde et al. (2011) detect o-H_2O $1_{10} \rightarrow 1_{01}$ and p-H_2O $1_{11} \rightarrow 0_{00}$ emission from TW Hya at 538 and 269 μm, respectively, with *Herschel*-HIFI. They attribute this emission to a large reservoir of water vapor at $r >$ 50 AU from the central star. We do not detect emission from these H_2O transitions in our (relatively low sensitivity) SPIRE spectrum.

We also detect collisionally excited OH $^2\Pi_{3/2}$ emission toward V4046 Sgr at 119.23 and 119.44 μm in the PACS range spectra, along with radiatively excited OH $^2\Pi_{3/2}$ emission at 84.60 and 84.42 μm (blended with CO) in the PACS line spectra (Figures 3 and 4, respectively). Fedele et al. (2012, 2013) and Wampfler et al. (2010, 2013) detect H_2O and OH emission from protoplanetary disks around both low- and high-mass young stellar objects. Emission from both the collisionally excited $^2\Pi_{3/2}$ level, as well as the far-infrared radiatively excited OH $^2\Pi_{1/2}$ level, is seen in most systems. Fedele et al. (2013) also detect OH emission features toward protoplanetary disks around both low- and high-mass stars. Since emission from OH $^2\Pi_{1/2}$ transitions is not detected in the PACS range scan spectra of V4046 Sgr, we conclude that collisionally excited OH molecules may dominate emission around more evolved sources like V4046 Sgr, whereas far-infrared pumping and collisional excitations are both important processes in younger, less evolved systems.

4.4. [O I]

Emission from [O I] is well detected at 63.18 μm in the *Herschel*/PACS spectrum of V4046 Sgr (Figure 3, Table 2). [O I] emission arises in protoplanetary disks when UV radiation from the central T Tauri star photodissociates CO or OH molecules in the outer disk (Mamon et al. 1988; Aresu et al. 2012). Disk gas-mass estimates and other disk properties can be derived through observations of ^{12}CO and ^{13}CO emission (especially when these features are optically thin), so it is important to understand how the CO in a disk has been affected by such a UV field. Emission from [O I] has been detected around both T Tauri and Herbig Ae/Be stars (e.g., Mathews et al. 2010; Riviere-Marichalar et al. 2012a, 2012b; Fedele et al. 2013; Howard et al. 2013; Keane et al. 2014) and is also well detected in the *Herschel* spectrum of TW Hya (Thi et al. 2010). The [O I] luminosity at 63 μm from TW Hya is comparable to the luminosity we measure from V4046 Sgr, yet neither V4046 Sgr nor TW Hya show detectable 145 μm [O I] emission or 158 μm [C II] emission (Thi et al. 2010). Emission from 370.3 μm [C I] is also not detected in the V4046 Sgr disk, but a 3σ upper limit is reported in Table 2. This may suggest that UV radiation from the central stars in both systems is actively photodissociating CO and/or OH in the outer layers of the disk (Acke et al. 2005), with the excess C and/or H then being bound up in the form of carbon or hydrogen-bearing molecules.

Keane et al. (2014) used Herschel PACS to search for [O I] 63 μm emission from full disks (i.e., systems with no evidence for a disk gap), transition disks, and outflow systems in

[13] V4046 Sgr was observed with *Spitzer* for 30 and 14 s in the SH and LH mode, respectively, while TW Hya was observed, only in SH mode, for 120 and 600 s.

star-forming regions. They detect [O I] emission from 21 transitional disks and find that the strength of the [O I] lines is typically $\sim 1/2$ that of full disk sources. Of the stars in the Keane et al. (2014) sample, V4046 Sgr is most similar to the full disk systems DK Tau, DQ Tau, DS Tau, DG Tau, and HK Tau in Taurus in terms of spectral type, multiplicity, and accretion rate. Assuming a distance to Taurus of 137 pc (Torres et al. 2008), we find that the luminosity of the [O I] line for V4046 Sgr is $\sim 1/4$ that of these Taurus star/disk systems, consistent with the notion that transitional disk systems tend to have lower [O I] line strengths (Keane et al. 2014).

4.5. HCN

HCN serves as a tracer of carbon-rich disk regions, where there is an excess of carbon to bond with free H and N atoms. Normally, most of the carbon is bound in either CO or CO_2 molecules, but in disks with a high H_2O content, much of the oxygen is locked up in H_2O, leaving behind excess C (Agúndez et al. 2008). Emission from mid-IR HCN is commonly seen in T Tauri stars (Pontoppidan et al. 2009) and is potentially correlated with accretion rate and X-ray luminosity (Teske et al. 2011). We detect emission from HCN at ~ 14 μm in the *Spitzer* spectrum of V4046 Sgr (Figure 1). The integrated HCN line flux is comparable to HCN emission from classical T Tauri stars in Taurus (3.2 mJy μm; Teske et al. 2011). HCN has previously been detected around V4046 Sgr at sub-millimeter wavelengths with the IRAM 30m and APEX telescopes (Kastner et al. 2008, 2014) and this sub-millimeter emission may also be correlated with UV/X-ray luminosity (Kastner et al. 2008).

4.6. CO

CO emission from the outer ($R \gtrsim 30$ to ~ 370 AU) disk of V4046 Sgr has previously been detected in the sub-millimeter with the SMA (Rodriguez et al. 2010) and IRAM (Kastner et al. 2008) and was extensively modeled by Rosenfeld et al. (2013). The *Herschel*/PACS data extend these CO detections to higher-J transitions that probe the warmer inner regions of the disk ($R \sim 10$–30 AU). The PACS line scan data (Figure 4) show emission from high-J transitions of CO that are not apparent in the less sensitive range scan PACS data (Figure 2). Specifically, we detect emission from CO $J = 31 \rightarrow 30$ (blended with OH), $18 \rightarrow 17$, and $15 \rightarrow 14$ and tentatively detect emission from CO $J = 30 \rightarrow 29$. Modeling of these *Herschel*/PACS CO emission features, along with the other emission features mentioned above and previous studies of CO emission, would help constrain the gas temperature distribution throughout the V4046 Sgr disk.

5. SILICATE DUST

5.1. Dust Grain Modeling

Silicate grain spectral emission features, including amorphous silicates, as well as crystalline grain species such as forsterite, enstatite, silica, pyroxene, and olivine, have been identified in the mid-IR spectra of many T Tauri stars (e.g., Cohen & Witteborn 1985; Honda et al. 2003; Sargent et al. 2006, 2009a). Analysis of such spectra yields dust grain compositions and, in particular, the type and relative concentrations of silicates in these disks. We modeled the silicate dust features in the *Spitzer* IRS spectrum of V4046 Sgr using custom IDL programs developed by Sargent et al. (2009b). In this method, one fits a two-temperature model that is the sum of optically thick emission from warm and cold blackbodies (T_w and T_c, respectively) and optically thin emission from two dust populations corresponding to T_w and T_c, respectively. The model flux is given by

$$F_\nu(\lambda)^{\rm mod} = B_\nu(\lambda, T_c)\left[\Omega_c + \sum_j a_{c,j}\kappa_j(\lambda)\right] + B_\nu(\lambda, T_w)\left[\Omega_w + \sum_j a_{w,j}\kappa_j(\lambda)\right], \quad (2)$$

where $B_\nu(\lambda, T)$ is the Planck function, Ω_c (Ω_w) is the solid angle of the blackbody at temperature T_c (T_w), $a_{c,j}$ ($a_{w,j}$) is the mass weight of silicate dust feature j at temperature T_c (T_w), and $\kappa_j(\lambda)$ is the opacity at wavelength λ for dust species j. While a multi-temperature model would be more realistic, a two-temperature dust model that characterizes the inner and outer disk regions generally well describes the thermal IR emission from T Tauri star disks (Sargent et al. 2009a). To determine the best-fit model to the V4046 Sgr spectrum, we minimize χ^2 between the model and the 7.7–33 μm region of the spectrum. It is assumed, for simplicity, that all data points are independent (i.e., the covariance between pixels is zero). Our *Spitzer* data are excessively noisy longward of 33 μm, so we omit these data from the fit. The best-fit model (Table 3), which has 18 free parameters fitting 1490 individual data points, is shown in Figure 7. This model spectrum assumes a central source of blackbody temperature 4200 K and indicates that the temperature of dust detected by *Spitzer* lies in the range $\sim$120–340 K.

Table 3
Model Dust Mass Percentages in the V4046 Sgr Disk

Dust Type	% by Mass
Cool large amorphous pyroxene	20.01% ± 5.79%
Cool large amorphous olivine	65.93% ± 8.44%
Cool forsterite	6.96% ± 3.24%
Cool silica	7.09% ± 3.54%
Warm large amorphous olivine	96.89% ± 15.55%
Warm forsterite	3.11% ± 4.33%
Cool crystalline silicates	14.05% ± 5.83%
Warm crystalline silicates	3.11% ± 7.99%
Total large silicates	85.96% ± 10.20%

5.2. Dust Composition

Table 3 lists the main results of the model fitting just described, in the form of the percent by mass of warm and cool dust grain species responsible for the mid-IR emitting region of the disk around V4046 Sgr. Note that this model does not include carbon or other dust grain species with featureless mid-IR spectra that contribute to the continuum emission. The modeling indicates that the silicate dust in the inner disk is primarily (86% by mass) composed of large (~ 5 μm radius) amorphous pyroxene and olivine grains at both warm and cool temperatures. There are also clear signatures of warm and cool forsterite and silica in crystalline form; these grain types

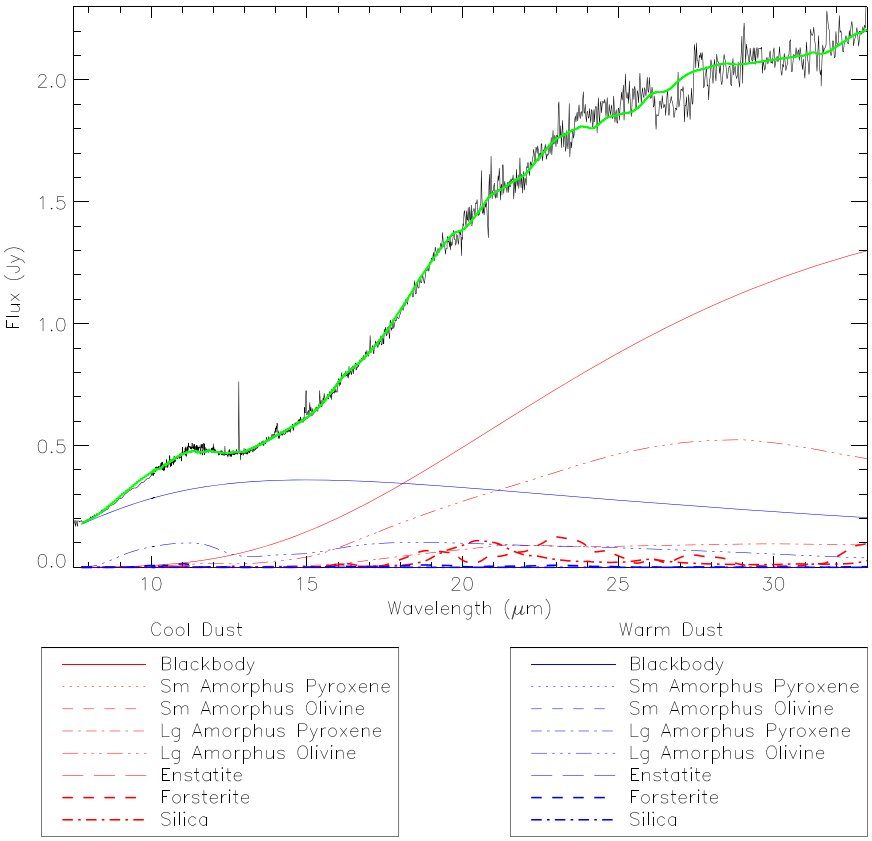

Figure 7. *Spitzer* IRS spectra (black) with best-fit silicate model overlaid (green). The cool dust components of the model are shown in red, and the warm dust components are shown in blue.

constitute the other 14% of the total silicate dust composition, according to the model fitting. The modeling indicates that contributions to the mid-IR emission from small grains below the Rayleigh limit ($2\pi a/\lambda \ll 1$, where a is the radius of the dust grain) or other non-crystalline components are negligible.

The foregoing results allow us to compare the composition of the dust in the circumbinary disk orbiting V4046 Sgr with other protoplanetary disks and other transitional disk objects of similar age, such as TW Hya and Hen 3-600 (TWA 3). Modeling of the *Spitzer* IRS spectra of TW Hya implies a large silicate grain fraction of ∼34.4%, with only 2.5% crystallinity, while modeling of Hen 3-600A results in a similar large silicate grain percentage of 31.9%, but with a high crystallinity of 36.2% (Honda et al. 2003; Sargent et al. 2006). Studies of T Tauri stars in the Taurus/Auriga star-forming region and the TW Hydrae association have shown that these transitional disk systems have negligible crystallinity and only modest large silicate grain fractions (<35%; Sargent et al. 2006), yet the disk around V4046 Sgr has a comparatively high crystallinity fraction and is otherwise dominated by large silicate grains.

Sargent et al. (2009a) use methods identical to those described above to model the *Spitzer* spectrum of 64 protoplanetary disks in the Taurus/Auriga star-forming region (age ∼1–2 Myr; Kenyon & Hartmann 1995), which is considerably younger than V4046 Sgr. They find median mass fractions for warm and cool crystalline silicate dust of 11% and 15%, respectively, whereas V4046 Sgr displays 3% and 14% crystallinity, respectively. However, the transitional and pre-transitional sources in the Sargent et al. (2009a) sample all have negligible crystallinity fractions. The fraction of large, cool dust grains inferred for the V4046 Sgr disk is also very high—larger than 93% of the sources in Taurus/Auriga. This suggests that grain growth has occurred in the disk, which is consistent with the advanced age of the system. Sargent et al. (2009a) also find that disks orbiting multiple-star systems tend to have larger warm large grain fractions than single-star systems. This may be due to dynamical interactions between the stars and the disk that trigger grain growth in the inner disk and/or to photoevaporation of small grains. Since V4046 Sgr is a multiple-star system with a large mass fraction of cool large grains rather than warm large grains, it is possible that a planetary companion in the inner disk is clearing away smaller particles and enhancing the large grain population at larger (cooler) radii.

A variety of mechanisms have been suggested as to how crystalline silicates form in protoplanetary disks (see, e.g., Sargent et al. 2006). One of the leading mechanisms involves amorphous silicates being thermally annealed into crystalline silicates as a result of heating induced by shock fronts within the disk. These shock fronts can result from star–disk interactions, if the disk is massive enough, or from local gravitational instabilities associated with planet formation. Rapson et al. (2015) present direct-imaging evidence for dust segregation by size, as well as dust ring structure, in the inner ∼40 AU of the disk around V4046 Sgr, and suggest that planet formation has occurred or is ongoing in the disk. This planet formation activity, if present, would help explain the combination of moderate crystallinity and large dust grains. Grain growth and planet formation may have occurred recently in the disk, thus creating a larger than typical crystallinity

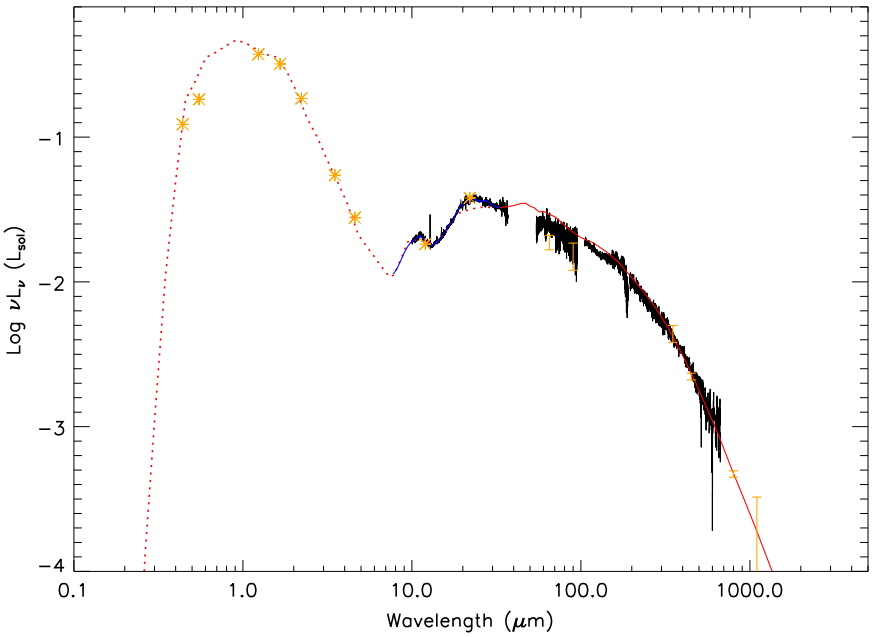

Figure 8. *Spitzer* and *Herschel* spectra (black) with our silicate dust model (blue) from 7 to 33 μm and the Rosenfeld et al. (2013) model (red solid) from 33 to 600 μm overlaid. The Rosenfeld et al. (2013) model from 0.25 to 33 μm is shown as the red dotted line. Orange asterisks are photometric data points from the literature (B and V from Høg et al. 2000; I from Messina et al. 2010; J, H, and K from Cutri et al. 2003; *AKARI* 65 and 90 μm data from Yamamura et al. 2010; *WISE* bands 1–4 data from Cutri 2013; and 350, 450, 800, and 1100 μm data from Jensen et al. 1996).

fraction for a disk with an inner gap and advanced age. Crystalline silicates at or interior to these planet formation zones would likely accrete onto either the central binary star or protoplanet(s). Since the *Spitzer* spectra are tracing the inner few AU of the disk, we may be seeing the crystalline silicates in the innermost portion of the disk that have not yet accreted onto the central stars.

Another possible scenario for the presence of crystalline silicates in the disk, and the varying crystallinity fraction among young stars, is thermal annealing of surface grains due to intense pre-MS stellar outbursts (Ábrahám et al. 2009). Such outbursts are typically associated with episodes of dramatically enhanced pre-MS accretion rate, however, and the (highly evolved, low-accretion-rate) V4046 Sgr system is unlikely to have experienced such an episode. Furthermore, our modeling shows that the warm dust is currently at a temperature of ∼350 K, far below the ∼700 K required to thermally anneal dust, so if crystalline silicates formed via irradiation during an accretion-related outburst, they have since cooled and migrated outward in the disk.

5.3. Amending the Rosenfeld et al. (2013) Model

Modeling of the entire V4046 Sgr disk was conducted by Rosenfeld et al. (2013) based on their SMA CO data, as well as on *Spitzer* IRS spectra and archival photometric data of V4046 Sgr. Using a 3D radiative transfer code, they developed a three-component model that includes an inner "gap" filled with μm-sized dust grains out to ∼30 AU, a ring of centimeter/millimeter-sized dust grains from ∼30–45 AU, and an extended halo of CO and small grain emission. Their resulting model well reproduces the mid- to far-IR photometry and 1.3 mm ^{12}CO and continuum interferometric observations of V4046 Sgr. The same model fits our *Herschel* data remarkably well, due to their inclusion of μm-sized grains out to ∼30 AU. However, the Rosenfeld et al. (2013) model did not reproduce the detailed SED structure at *Spitzer* IRS wavelengths. The mismatch between the model and data in this wavelength range was due to the presence of a complex (crystalline plus amorphous) silicate grain mixture in the inner disk that is not accounted for by the three-component model.

In Figure 8, we replace the shorter-wavelength (7.7–33 μm) portion of the Rosenfeld et al. (2013) model with our silicate model. This revised model, which better reproduces the *Spitzer* spectra, merges seamlessly with the Rosenfeld model at ∼33 μm. Using the Rosenfeld et al. (2013) model, we can estimate the characteristic disk radii probed by our silicate model, assuming that our newly calculated dust composition and resulting dust opacities do not significantly alter the disk temperature in their models. Figure 9 shows disk temperature versus radius for both large (millimeter-sized) and small (micron-sized) grains based on the Rosenfeld et al. (2013) model. Our silicate dust modeling shows dust at 340 and 116 K, which correspond to a radius of 0.3 and 1.3 AU, respectively, for small (μm-sized) grains. We conclude that the *Spitzer* data likely probe the dust grain populations of the inner disk within these approximate radii.

6. CONCLUSIONS

We have presented an analysis of *Spitzer* and *Herschel* spectra of the disk around V4046 Sgr that elucidates the gas and dust constituents within the disk. We confirm the measurement of strong [Ne II] at 12.8 μm previously reported by Sacco et al. (2012) and report an upper limit for [Ne III] emission. The [Ne III]/[Ne II] ratio is consistent with other CTTS systems that are X-ray bright and lack jets. We also detect emission from pure rotational H_2 0-0 S(1) ($J = 3 \rightarrow 1$) at 17 μm that likely originates in the surface layers of the disk where the temperature is warmer than the midplane at a given radius due to stellar UV/X-ray irradiation.

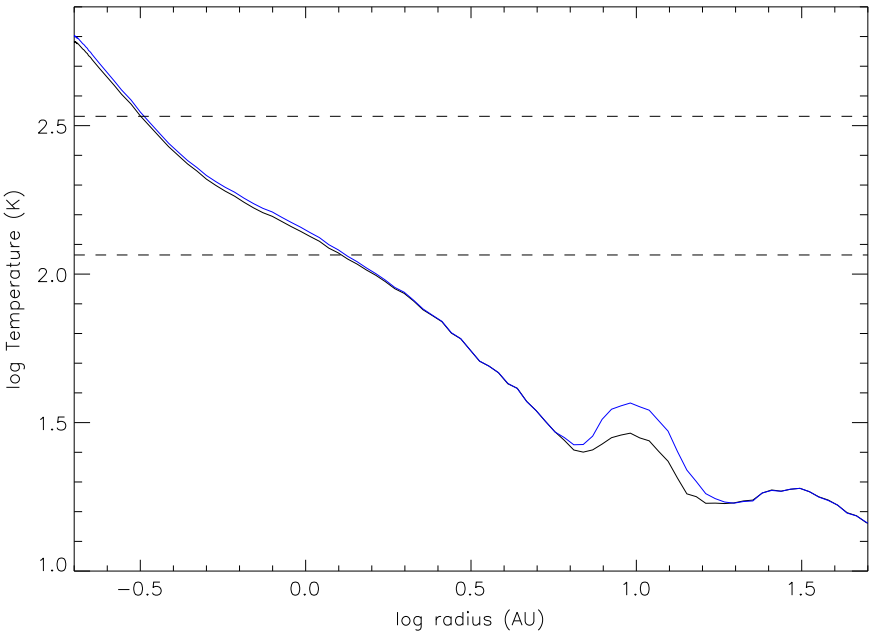

Figure 9. Temperature at a given disk radius in the Rosenfeld et al. (2013) model for large grains ($R > 5$ μm; black solid line) and small grains ($R \sim 5$ μm; blue solid line). The horizontal dashed lines at 340 and 116 K represent the two temperatures of the micron-sized silicate dust grains in our model.

The X-ray/UV radiation coming from the central binary is likely photodissociating CO, H_2O, and OH, resulting in emission from [O I] and OH. We detect emission from [O I] at 63 μm, but do not detect [C I] or [C II] in the mid- to far-infrared. Thus, the excess C atoms may be forming HCN and other hydrocarbons throughout the disk, and/or the [O I] is arising from photodissociated OH in the disk. The strength of the [O I] emission is lower than that for star–disk systems of similar spectral type and accretion properties surrounded by continuous disks, as was found by Keane et al. (2014) and Howard et al. (2013). V4046 Sgr exhibits OH $^2\Pi_{3/2}$ emission at 84.4, 84.6, and 119 μm, and possible weak H_2O emission features in the mid- to far-infrared. This suggests that H_2O and collisionally excited OH molecules reside in the the outer layers of the V4046 Sgr disk.

Modeling of the *Spitzer* spectra reveal that the mid-IR emitting region of the disk consists primarily of large ($\sim$5 μm) silicate dust particles (86% by mass), with crystalline forsterite and silica particles making up the other 14% of the mass. Overall, the presence of large grains suggests that grain growth may be occurring in the inner $\sim$30 AU gap around V4046 Sgr and the abundance of cool dust suggests that dust may be settling toward the midplane where temperatures are lower at a given radius. The moderate crystallinity fraction is similar to that of less evolved protoplanetary disks in the Taurus/Auriga star-forming region (Sargent et al. 2009a) and may result from heating and thermal annealing of micron-sized dust that is associated with planet formation activity in the inner disk (Rapson et al. 2015). Combining our silicate dust model with the mid-IR to sub-millimeter three-component model of Rosenfeld et al. (2013), we find that the dust emission seen in the *Spitzer* spectrum likely originates from regions of the disk interior to 1.3 AU. These results together suggest that grain growth might, in part, explain the transitional appearance of this disk.

We would like to thank Katrina Exter for assistance with processing the PACS and SPIRE data, as well as Wing Fai Thi and Dan Watson for their helpful discussions. We would also like to thank the anonymous reference for helpful suggestions which greatly improved the manuscript. This research work is based in part on observations made with *Herschel*, a European Space Agency Cornerstone Mission with significant participation by NASA; support was provided by NASA through an award to R.I.T. issued by JPL/Caltech. Additional support is provided by National Science Foundation grant AST-1108950 to R.I.T.

REFERENCES

Ábrahám, P., Juhász, A., Dullemond, C. P., et al. 2009, Natur, 459, 224
Acke, B., van den Ancker, M. E., & Dullemond, C. P. 2005, A&A, 436, 209
Agúndez, M., Cernicharo, J., & Goicoechea, J. R. 2008, A&A, 483, 831
Alexander, R., Pascucci, I., Andrews, S., Armitage, P., & Cieza, L. 2014, Protostars and Planets VI (Tuscon, AZ: Univ. Arizona Press)
Aresu, G., Meijerink, R., Kamp, I., et al. 2012, A&A, 547, A69
Argiroffi, C., Maggio, A., Montmerle, T., et al. 2012, ApJ, 752, 100
Bary, J. S., Weintraub, D. A., Shukla, S. J., Leisenring, J. M., & Kastner, J. H. 2008, ApJ, 678, 1088
Bergin, E., Calvet, N., D'Alessio, P., & Herczeg, G. J. 2003, ApJL, 591, L159
Binks, A. S., & Jeffries, R. D. 2013, MNRAS (arXiv:1310.2613)
Bitner, M. A., Richter, M. J., Lacy, J. H., et al. 2008, ApJ, 688, 1326
Bruderer, S., van Dishoeck, E. F., Doty, S. D., & Herczeg, G. J. 2012, A&A, 541, A91
Calvet, N., Patino, A., Magris, G. C., & D'Alessio, P. 1991, ApJ, 380, 617
Carmona, A., van den Ancker, M. E., Henning, T., et al. 2008, A&A, 478, 795
Carr, J. S., & Najita, J. R. 2008, Sci, 319, 1504
Carr, J. S., & Najita, J. R. 2011, ApJ, 733, 102
Cleeves, L. I., Bergin, E. A., Bethell, T. J., et al. 2011, ApJL, 743, L2
Cohen, M., & Witteborn, F. C. 1985, ApJ, 294, 345
Cutri, R. M., Wright, E. L., Conrow, T., et al. 2013, yCat, 2328, 0
Cutri, R. M., Skrutskie, M. F., van Dyk, S., et al. 2003, 2MASS All Sky Catalog of Point Sources
Donati, J.-F., Gregory, S. G., Montmerle, T., et al. 2011, MNRAS, 417, 1747
Ducourant, C., Teixeira, R., Chauvin, G., et al. 2013, in IAU Symp. 289, Advancing the Physics of Cosmic Distances, ed. R. de Grijs (Cambridge: Cambridge Univ. Press), 386
Ercolano, B., Drake, J. J., Raymond, J. C., & Clarke, C. C. 2008, ApJ, 688, 398
Ercolano, B., & Owen, J. E. 2010, MNRAS, 406, 1553

Espaillat, C., Calvet, N., D'Alessio, P., et al. 2007, ApJL, 664, L111
Fedele, D., Bruderer, S., van Dishoeck, E. F., et al. 2012, A&A, 544, L9
Fedele, D., Bruderer, S., van Dishoeck, E. F., et al. 2013, A&A, 559, A77
Feigelson, E. D., Casanova, S., Montmerle, T., & Guibert, J. 1993, ApJ, 416, 623
Glassgold, A. E., Najita, J., & Igea, J. 2004, ApJ, 615, 972
Griffin, M. J., Abergel, A., Abreu, A., et al. 2010, A&A, 518, L3
Güdel, M., Lahuis, F., Briggs, K. R., et al. 2010, A&A, 519, A113
Henning, T., Semenov, D., Guilloteau, S., et al. 2010, ApJ, 714, 1511
Higdon, S. J. U., Devost, D., Higdon, J. L., et al. 2004, PASP, 116, 975
Høg, E., Fabricius, C., Makarov, V. V., et al. 2000, A&A, 355, L27
Hogerheijde, M. R., Bergin, E. A., Brinch, C., et al. 2011, Sci, 334, 338
Honda, M., Kataza, H., Okamoto, Y. K., et al. 2003, ApJL, 585, L59
Houck, J. R., Roellig, T. L., Van Cleve, J., et al. 2004, Proc. SPIE, 5487, 62
Howard, C. D., Sandell, G., Vacca, W. D., et al. 2013, ApJ, 776, 21
Hughes, A. M., Wilner, D. J., Calvet, N., et al. 2007, ApJ, 664, 536
Jensen, E. L. N., Mathieu, R. D., & Fuller, G. A. 1996, ApJ, 458, 312
Kastner, J. H., Hily-Blant, P., Rodriguez, D. R., Punzi, K., & Forveille, T. 2014, ApJ, 793, 55
Kastner, J. H., Zuckerman, B., Hily-Blant, P., & Forveille, T. 2008, A&A, 492, 469
Keane, J. T., Pascucci, I., Espaillat, C., et al. 2014, ApJ, 787, 153
Kenyon, S. J., & Hartmann, L. 1995, ApJS, 101, 117
Lahuis, F., van Dishoeck, E. F., Blake, G. A., et al. 2007, ApJ, 665, 492
Malbet, F., & Bertout, C. 1991, ApJ, 383, 814
Mamajek, E. E., & Bell, C. P. M. 2014, MNRAS, 445, 2169
Mamon, G. A., Glassgold, A. E., & Huggins, P. J. 1988, ApJ, 328, 797
Mathews, G. S., Dent, W. R. F., Williams, J. P., et al. 2010, A&A, 518, L127
Meeus, G., Salyk, C., Bruderer, S., et al. 2013, arXiv:1308.4160
Meijerink, R., Glassgold, A. E., & Najita, J. R. 2008, ApJ, 676, 518
Meijerink, R., Pontoppidan, K. M., Blake, G. A., Poelman, D. R., & Dullemond, C. P. 2009, ApJ, 704, 1471
Messina, S., Desidera, S., Turatto, M., Lanzafame, A. C., & Guinan, E. F. 2010, A&A, 520, A15
Najita, J. R., Carr, J. S., Strom, S. E., et al. 2010, ApJ, 712, 274
Najita, J. R., Crockett, N., & Carr, J. S. 2008, ApJ, 687, 1168
Ott, S. 2010, in ASP Conf. Ser. 434, Astronomical Data Analysis Software and Systems XIX, ed. Y. Mizumoto, K.-I. Morita & M. Ohishi (San Francisco, CA: ASP), 139
Pascucci, I., Apai, D., Luhman, K., et al. 2009, ApJ, 696, 143
Pascucci, I., Herczeg, G., Carr, J. S., & Bruderer, S. 2013, ApJ, 779, 178
Pascucci, I., Hollenbach, D., Najita, J., et al. 2007, ApJ, 663, 383
Pascucci, I., Ricci, L., Gorti, U., et al. 2014, ApJ, 795, 1
Pilbratt, G. L., Riedinger, J. R., Passvogel, T., et al. 2010, A&A, 518, L1
Poglitsch, A., Waelkens, C., Geis, N., et al. 2010, A&A, 518, L2
Pontoppidan, K. M., Meijerink, R., Dullemond, C. P., & Blake, G. A. 2009, ApJ, 704, 1482
Pontoppidan, K. M., Salyk, C., Bergin, E. A., et al. 2014, Protostars and Planets VI (Tuscon, AZ: Univ. Arizona Press)
Pontoppidan, K. M., Salyk, C., Blake, G. A., et al. 2010, ApJ, 720, 887
Rapson, V. A., Kastner, J. H., Andrews, S. M., et al. 2015, ApJL, 803, L10
Rigliaco, E., Pascucci, I., Duchene, G., et al. 2015, ApJ, 801, 31
Riviere-Marichalar, P., Barrado, D., Augereau, J.-C., et al. 2012a, A&A, 546, L8
Riviere-Marichalar, P., Ménard, F., Thi, W. F., et al. 2012b, A&A, 538, L3
Riviere-Marichalar, P., Pinte, C., Barrado, D., et al. 2013, A&A, 555, A67
Rodriguez, D. R., Kastner, J. H., Wilner, D., & Qi, C. 2010, ApJ, 720, 1684
Rosenfeld, K. A., Andrews, S. M., Wilner, D. J., Kastner, J. H., & McClure, M. K. 2013, ApJ, 775, 136
Rosenfeld, K. A., Andrews, S. M., Wilner, D. J., & Stempels, H. C. 2012a, ApJ, 759, 119
Rosenfeld, K. A., Qi, C., Andrews, S. M., et al. 2012b, ApJ, 757, 129
Sacco, G. G., Flaccomio, E., Pascucci, I., et al. 2012, ApJ, 747, 142
Salyk, C. 2011, in IAU Symp. 280, The Molecular Universe, ed. J. Cernicharo & R. Bachiller (Cambridge: Cambridge Univ. Press), 127
Salyk, C., Pontoppidan, K. M., Blake, G. A., Najita, J. R., & Carr, J. S. 2011, ApJ, 731, 130
Salyk, C., Pontoppidan, K. M., Blake, G. A., et al. 2008, ApJL, 676, L49
Sargent, B., Forrest, W. J., D'Alessio, P., et al. 2006, ApJ, 645, 395
Sargent, B. A., Forrest, W. J., Tayrien, C., et al. 2009a, ApJS, 182, 477
Sargent, B. A., Forrest, W. J., Tayrien, C., et al. 2009b, ApJ, 690, 1193
Stempels, H. C., & Gahm, G. F. 2004, A&A, 421, 1159
Takahashi, J. 2001, ApJ, 561, 254
Teske, J. K., Najita, J. R., Carr, J. S., et al. 2011, ApJ, 734, 27
Thi, W.-F., Mathews, G., Ménard, F., et al. 2010, A&A, 518, L125
Thi, W. F., van Dishoeck, E. F., Blake, G. A., et al. 2001, ApJ, 561, 1074
Torres, C. A. O., Quast, G. R., da Silva, L., et al. 2006, A&A, 460, 695
Torres, C. A. O., Quast, G. R., Melo, C. H. F., & Sterzik, M. F. 2008, in Young Nearby Loose Associations, ed. B. Reipurth (San Francisco, CA: ASP), 757
Wampfler, S. F., Bruderer, S., Karska, A., et al. 2013, A&A, 552, A56
Wampfler, S. F., Herczeg, G. J., Bruderer, S., et al. 2010, A&A, 521, L36
Werner, M. W., Roellig, T. L., Low, F. J., et al. 2004, ApJS, 154, 1
Wolniewicz, L., Simbotin, I., & Dalgarno, A. 1998, ApJS, 115, 293
Yamamura, I., Makiuti, S., Ikeda, N., et al. 2010, yCat, 2298, 0